GA–A24687

MHD EQUILIBRIUM RECONSTRUCTION IN THE DIII–D TOKAMAK

by

L.L. LAO, H.E. St JOHN, Q. PENG, J.R. FERRON, W.H. MEYER,
E.J. STRAIT, T.S. TAYLOR, K.I. YOU, and C. ZHANG

APRIL 2004

DISCLAIMER

GA–A24687

MHD EQUILIBRIUM RECONSTRUCTION IN THE DIII–D TOKAMAK

by
L.L. LAO, H.E. St JOHN, Q. PENG, J.R. FERRON, W.H. MEYER,*
E.J. STRAIT, T.S. TAYLOR, K.I. YOU,† and C. ZHANG‡

This is a preprint of a paper to be submitted for publication in a special issue of *Fusion Science and Technology.*

*Lawrence Livermore National Laboratory, Livermore, California
†Institute of Plasma Physics, Chinese Academy of Science, Hefei, China
‡National Fusion Research Center, Korean Basic Science Institute, Daejeon, Korea

Work supported by
the U.S. Department of Energy
under DE-FC02-04ER54698 and W-7405-ENG-48

GENERAL ATOMICS PROJECT 30200
APRIL 2004

ABSTRACT

Physics elements and advances crucial for the development of axisymmetric magnetohydrodynamic (MHD) equilibrium reconstruction to support plasma operation and data analysis in the DIII-D tokamak are reviewed. A response function formalism and a Picard linearization scheme are used to efficiently combine the equilibrium and the fitting iterations and search for the optimum solution vector. Algorithms to incorporate internal current and pressure profile measurements, topological constraints, and toroidal plasma rotation into the equilibrium reconstruction are described. Choice of basis functions and boundary conditions essential for accurate reconstruction of L- and H-mode equilibrium plasma boundary and current and pressure profiles are discussed. The computational structure used to efficiently integrated these elements into the equilibrium reconstruction code EFIT is summarized.

I. INTRODUCTION AND OVERVIEW

Reconstruction of experimental axisymmetric magnetohydrodynamic (MHD) equilibria is an important part of tokamak data analysis and has contributed significantly to several major discoveries of tokamak physics such as the experimental validation of theoretically predicted β stability limits and the negative central shear operating regime. It is routinely used for plasma shape control and to support plasma operation and data analysis. In this paper, physics elements and advances that are crucial to the development of equilibrium reconstruction in the DIII-D tokamak and relevant for the next step burning plasma experiments such as the International Thermonuclear Experimental Reactor (ITER) are reviewed and discussed.

The first pioneering tokamak equilibrium reconstructions were carried out to analyze data for the Doublet III tokamak on an array processor using external magnetic data with a conventional equilibrium code [1]. This work demonstrated that in a non-circular tokamak, external magnetic measurements outside the plasma can determine both the plasma stored energy and the current profile peakedness, in addition to the plasma shape. The reconstruction required many equilibrium calculations and is computationally expensive. The positive results from this work and the subsequent strong demands for data analysis motivated the development of the filament current magnetic fitting code MFIT [2] and later the equilibrium fitting code EFIT [3] during the last phase of Doublet III operation. MFIT uses filament currents to model the plasma current profile. It, therefore, is computationally very inexpensive but suffers from lack of accuracy in describing the plasma flux surfaces [2]. This computationally efficient technique was first developed by Swain and Neilson to support magnetic analysis in the ISX-B tokamak [4]. The positive ISX-B results motivated the development of MFIT for DIII-D.

EFIT retains the computational efficiency of the filament code approach by interleaving the equilibrium and the fitting iterations with a Picard linearization scheme to find the optimum solution, but improves on the accuracy by allowing for a distributed plasma current source constrained by MHD equilibrium [3]. The equilibrium constraint allows the two-dimensional

toroidal current density J_ϕ to be represented using two one-dimensional stream functions that significantly reduce the complexity of the problem. The nonlinear optimization problem is efficiently solved by transforming into a sequence of linear problems using approximate magnetic geometry information from previous iterations to linearize the plasma response. All available measurements are appropriately weighted with an uncertainty vector to account for the measurement errors and incorporated into a single response matrix that relates them to the current source through the Green induction functions. The use of the uncertainty vector allows all available data to be flexibly included or entirely left out in the reconstruction. This flexibility is essential when it is used in conjunction with plasma operation.

The use of the response function approach allows the lengthy calculations of the inductance matrix to be separated from the rapid reconstruction iterations. The Green induction functions can be pre-computed and stored in look-up tables. This, together with advances in computer hardware, substantially reduce the amount of computational effort required and make possible equilibrium reconstruction of a whole discharge between plasma shots, as well as real-time equilibrium reconstruction for plasma control [5]. To increase the flexibility in the magnetic configurations allowed, a cylindrical (R, ϕ, Z) coordinate system is used in EFIT with the vertical Z-axis pointing in the direction of the torus axis of symmetry, rather than one based on magnetic flux surfaces. This allows an accurate representation of the divertor geometry. Here, R and ϕ are the major radius and the toroidal angle of the torus.

External magnetic measurements, although essential to the equilibrium reconstruction, alone can only yield global current and pressure profile parameters such as poloidal plasma beta $\beta_p = 2\mu_0 \int_\Omega dV\, P \Big/ \left(B_{pa}^2 \Omega\right)$ and internal plasma inductance $\ell_i = \int_\Omega dV\, B_p^2 \Big/ \left(B_{pa}^2 \Omega\right)$ [1–3,6–8]. Here, Ω is the plasma volume, $B_{pa} = \mu_0 I_p \Big/ \int_\Gamma d\ell$ is an average poloidal magnetic field for normalization, and Γ denotes the plasma surface bounding Ω. To fully reconstruct the pressure and current profiles and the associated magnetic topology self-consistently, internal current and kinetic profile measurements must be used in conjunction with external magnetic data.

In DIII-D, internal current profile information is provided by the motional Stark effect (MSE) diagnostic [9–11], which measures the local pitch angles of the magnetic field lines inside the plasma using a spectroscopic technique. Information on P is provided by the density and

temperature profile measurements from Thomson scattering (TS), electron cyclotron emission (ECE), and charge exchange recombination (CER) diagnostics together with a theoretically computed fast ion pressure component for neutral-beam heated plasmas [12]. The temperature profile measurement also provides useful information on the topology of the internal magnetic surfaces that can be used to further constrain the equilibrium reconstruction [13,14].

In high confinement H-mode discharges, the edge radial electric fields can be large. This can introduce a large uncertainty into the reconstructed edge current density profile [15,16]. A new Li beam diagnostic based on the Zeeman effect has recently been deployed in DIII-D to improve the measurement of the edge current density profile [17]. Since the Zeeman effect is not sensitive to the radial electric field and has greater signal strength, the Li beam diagnostic can provide a more accurate determination of the edge current profile. The Li beam measurements can be incorporated into the response matrix using linearization schemes similar to those developed for the MSE diagnostic.

Proper boundary conditions and representation of pressure and current profiles are crucial for accurate reconstruction of equilibrium magnetic surfaces and current and pressure profiles. For Ohmic and L-mode discharges, a simple polynomial representation of the pressure and current density profiles plus zero edge pressure gradient and current density boundary conditions are usually sufficient to accurately reconstruct the plasma boundary and equilibrium. For H-mode plasmas, due to the large edge pressure gradient and the associated bootstrap and diamagnetic current density, the edge boundary pressure gradient and current density must be allowed to have finite values to accurately reconstruct the plasma boundary and equilibrium. In EFIT, both zero and finite edge pressure gradient and current density boundary conditions can be conveniently imposed through the use of a boundary condition weighting vector.

In the presence of toroidal rotation, the MHD equilibrium is constrained by two coupled partial differential equations describing force balance in the directions normal and tangential to a magnetic surface [18]. When the rotation energy is small, or when the plasma can be approximated as a simple ideal fluid, the tangential force balance equation can be integrated analytically, which significantly reduces the complexity of the problem. To reconstruct equilibria

with rotation, additional plasma mass density and toroidal rotation profile data must be used in conjunction with other data [19].

This paper is organized as follows. MHD equilibrium and fitting with external magnetic measurements are discussed in Section II. The use of internal current and kinetic profiles in the equilibrium reconstruction is discussed in Section III. The choice of boundary conditions and representation of current and pressure profiles and several illustrative examples are presented in Section IV. Equilibrium reconstruction with rotation is discussed in Section V. Various applications of equilibrium reconstruction to analyze and support DIII-D experiments using workstations and distributed Linux clusters and a summary are presented in Section VI.

II. MHD EQUILIBRIUM AND FITTING WITH EXTERNAL MAGNETIC DATA

In an axisymmetric toroidal system, the MHD equilibrium Grad-Shafranov equation can be written for a non-rotating plasma as

$$\Delta^* \psi = -\mu_0 R J_\phi \quad , \quad J_\phi = RP'(\psi) + \frac{\mu_0 FF'(\psi)}{4\pi^2 R} \quad . \tag{1}$$

Here, ψ is the poloidal magnetic flux per radian of the toroidal angle ϕ enclosed by a magnetic surface, $F = 2\pi RB_\phi / \mu_0$ and B_ϕ are the poloidal current function and the toroidal magnetic field, and $\Delta^* = R^2 \nabla \cdot \left(\nabla / R^2 \right)$. EFIT efficiently solves for the equilibrium numerically using the Picard iteration scheme by dividing $\psi = \psi_P + \psi_{ext}$ into a plasma and an external component, ψ_P and ψ_{ext}, separately computed using the differential and the integral forms of the equilibrium Eq. (1) [3].

As shown in Fig. 1, the DIII-D vacuum vessel is closely surrounded by 18 external shaping coils. The combined use of differential and integral approaches allows the rectangular (R, Z) computational domain to intersect the external coils and tightly fit the vacuum vessel. This significantly improves the spatial resolution of the equilibrium solution. The Δ^* operator is inverted using the fast Buneman double cyclic reduction method with ψ_P at the boundary of the computational domain constrained by the integral form of the equilibrium Eq. (1),

$$\psi_P(\bar{r}) = \int_\Omega dR' dZ' G_\psi(\bar{r}, \bar{r}') J_\phi \left[R', \psi(\bar{r}') \right] \quad . \tag{2}$$

Here, G_ψ is the Green induction function relating ψ to the current sources. This boundary condition can be straightforwardly incorporated into the iteration cycle using the Picard iteration scheme

$$\psi_P^{m+1}(\bar{r}) = \int_{\Omega^m} dR' dZ' G_\psi(\bar{r}, \bar{r}') J_\phi \left[R', \psi^m(\bar{r}') \right] \quad . \tag{3}$$

Here, m denotes the iteration cycle. Finite-size-coil effects are included in the external coil response function G_ψ in EFIT by representing the coils as a finite number of filament currents.

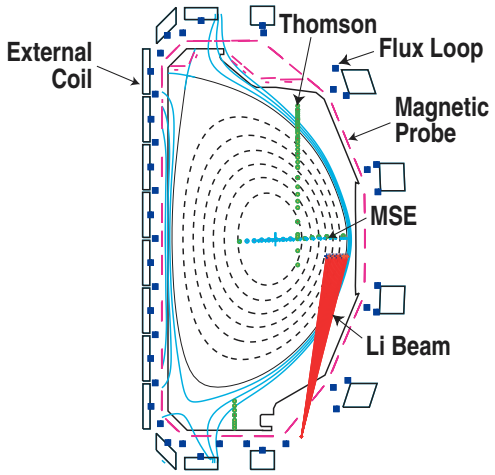

Fig. 1. A cross section of DIII-D summarizing in one plane the locations of the external coils, external magnetic probes, flux loops, internal MSE, Li beam, and Thomson scattering kinetic profile diagnostics.

A. External magnetic fitting

In an equilibrium reconstruction, the equilibrium Eq. (1) must be solved together with the available measurements as constraints on the plasma current source J_ϕ. To reconstruct the equilibrium, the two stream functions $P'(\psi)$ and $FF'(\psi)$ are represented using a set of basis functions, y_n, in terms of a number of linear parameters, α_n and γ_n, as

$$P'(\psi) = \sum_n \alpha_n y_n(x) \quad , FF'(\psi) = \sum_n \gamma_n y_n(x) \quad . \tag{4}$$

Here, $x = (\psi - \psi_0)/(\psi_1 - \psi_0)$ is the normalized poloidal magnetic flux, ψ_0 and ψ_1 are the poloidal magnetic flux at the magnetic axis and at the plasma boundary, and $0 \le x \le 1$. A polynomial, a spline representation, and a local representation are available in EFIT [20]. These will be further discussed in Section IV.

External magnetic measurements provide a key data set for the determination of the plasma boundary and current profile parameters such as I_p, β_p, and ℓ_i [1–3,6–8]. External magnetic measurements can be related to the plasma and the external coil currents through the Green induction function G_{Ci} and linearized using the Picard iteration scheme that approximates the magnetic geometry using information from the previous iteration as [3]

$$C_i^{m+1}(\bar{r}_i) = \sum_j G_{Ci}(\bar{r}_i, \bar{r}_{ej}) I_{ej} + \int_{\Omega^m} dR'\, dZ'\, G_{Ci}(\bar{r}_i, \bar{r}')\, J_\phi\left[R', \psi^m(\bar{r}'), \bar{\alpha}^{m+1}\right]. \tag{5}$$

Here, C_i is the computed value of the i^{th} magnetic measurement and the integration is carried out over the plasma volume. For a flux loop, $G_{Ci} = G_\psi$. I_{ej} is the total current in the j^{th} external coil located at $\bar{r}_{ej}$. The plasma boundary and ψ_1 are obtained by finding the largest closed flux surface (limiter) or separatrix surface enclosed by the surrounding limiter and vacuum vessel. In a normal discharge, P' and FF' are set to vanish in the vacuum region outside the plasma boundary.

During vertical displacement events (VDE), current can flow along the open magnetic field lines outside of the plasma boundary. This is modeled in EFIT using an attached current model by letting $x = (\psi - \psi_0)/(\psi_\mu - \psi_0)$ in the FF' term [21]. Here, ψ_μ is a poloidal flux parameter to describe the open field line attached current region outside of the plasma boundary, and $|\psi_\mu - \psi_0| \geq |\psi_1 - \psi_0|$.

The unknown parameters α_n and γ_n are then determined from all available magnetic data M_i by minimizing

$$\chi^2 = \sum_i \left(\frac{M_i - C_i}{\sigma_i} \right)^2 \quad . \tag{6}$$

Here, σ_i is the uncertainty associated with the i^{th} magnetic measurement.

B. Response matrix

Since the unknown parameters α_n and γ_n appear linearly, Eqs. (4) and (5) can be combined to explicitly relate the unknown parameter vector $\bar{\alpha}$ directly to the measurement vector $\bar{M}$ through the response matrix $\bar{\bar{R}}$ as

$$\bar{\bar{R}}\bar{\alpha} = \bar{M} \quad . \tag{7}$$

Here, the response matrix $\bar{\bar{R}}$ is an appropriate rearrangement of the Green induction functions and their integration over the plasma volume weighted by the uncertainties σ_i [3]. Note that in EFIT, rather than treating the external coil currents I_{ej} as given, $\bar{\alpha}$ consists of all the unknown plasma current profile parameters α_n and γ_n as well as the external coil currents I_{ej}. This approach allows all the magnetic and external coil current data to be consistently treated with their respective measurement uncertainties. For many modeling applications, it is useful to

impose a constraint on the axial safety factor value q_0 and the plasma boundary at certain points. These can be straightforwardly incorporated into $\overline{\overline{R}}$ using the Picard iteration scheme to linearize the dependence on $\overline{\alpha}$.

C. Benchmarking and tests

The DIII-D magnetic diagnostics consist of 67 magnetic probes located in two toroidal planes, 41 flux loops, 6 saddle loops, and 19 Rogowski loops to measure plasma and external coil currents. These are shown in Fig. 1. A very important part of the equilibrium reconstruction is the benchmarking of the external coil inductions against experimental measurements and the testing of the adequacy of the external magnetic diagnostic set for equilibrium reconstruction. A necessary condition for equilibrium reconstruction is that in the absence of the plasma the predicted magnetic responses from the external coils must agree with the experimental measurements within the measurement uncertainties. This is routinely done in DIII-D using vacuum shots.

III. RECONSTRUCTION WITH INTERNAL CURRENT AND KINETIC PROFILE MEASUREMENTS

To reconstruct the q profile, internal current profile measurements must be used in conjunction with the external magnetic data. In DIII-D, information on the internal current profile is provided by the MSE and Li beam diagnostics that use spectroscopic techniques to measure the local pitch angles of the magnetic field lines inside the plasma [16,17]. To fully reconstruct the equilibrium, kinetic profile data must be used in conjunction with the MSE, Li beam, and external magnetic data to reconstruct the q and pressure profiles and the associated magnetic geometry self-consistently [12].

A. MSE and Li beam internal current profile data

The MSE and the Li beam internal current profile measurements can be included in the equilibrium reconstruction by incorporating their linearized responses into $\overline{\overline{R}}$ using the Picard iteration scheme based on magnetic information from the previous iteration as

$$\left(A_{i1} - A_{i4}\tan\xi_i\right)B_Z^{m+1} + \left(A_{i8} - A_{i3}\tan\xi_i\right)B_R^{m+1}$$

$$-\left[D_{i1}B_Z^m - \left(D_{i2}B_Z^m + D_{i3}B_R^m\right)\tan\xi_i\right]\Phi'_E(\psi)^{m+1} = A_{i2}\tan\xi_i B_\phi^m \quad , \tag{8}$$

$$\Phi'_E(\psi)^{m+1} = \sum_n \eta_n^{m+1} y_n\left(x^m\right) \quad . \tag{9}$$

Here, A_{ik}, D_{ik}, and ξ_i are the geometric coefficients and the pitch angle associated with the ith MSE or Li beam measurements, and m again denotes the iteration cycle. B_R and B_Z are the R and Z components of the magnetic field that are related to the plasma and external coil currents through Eq. (5). $\Phi'_E(\psi)$ is the derivative of the electrostatic potential with respect to ψ that is related to the electric field by

$$\overline{E} = -\nabla\Phi_E \quad . \tag{10}$$

Note that D_{ik}'s are the correction terms to the MSE signals due to the radial electric field. They are not needed for the Li beam signals. In DIII-D, information on the radial electric field is provided using an MSE system with both radial and tangential views. The radial electric field profile reconstructed from equilibrium reconstruction using MSE data agrees well with that obtained from CER analysis of carbon impurities [16].

B. Kinetic pressure profile data

The pressure profile data can be related to the density and temperature profile measurements from TS, ECE, and CER plus the fast ion pressure P_f as [12]

$$P(x) = n_e(x)T_e(x) + \left[n_i(x) + n_z(x)\right] T_i(x) + P_f(x) \quad . \tag{11}$$

Here, n_e, n_i, and n_z are the electron, main ion, and impurity densities. T_e and T_i are the electron and main ion temperatures. The impurity temperature is taken to be the same as the main ion temperature. n_i and n_z are obtained from n_e from the quasi-neutrality condition and the Z_{eff} or impurity density measurement. These measurements are in different spatial locations in DIII-D. To form P, they are mapped into a common flux grid using magnetic geometry information from the previous iteration. In a neutral beam heated plasma, P_f is computed analytically using a standard classical slowing down model [12]. When there is substantial neutral beam heating, P_f can be large in the plasma core region. This may introduce a large systematic error into the reconstructed equilibrium current and pressure profiles in the plasma core, particularly when there are MHD instabilities that can radially re-distribute or expel the fast ions.

The pressure data can be included in the equilibrium reconstruction by incorporating the linearized pressure response into $\overline{\overline{R}}$ using magnetic geometry information from the previous iteration m as [12]

$$\sum_n \alpha_n^{m+1} \zeta\left(x_i^m\right) = \left(M_{Pi} - M_{P1}\right) \Big/ \left(\psi_1^m - \psi_0^m\right) \quad , \tag{12}$$

$$\zeta(x) = \int_{x1}^{x} y_n(x)dx \quad . \tag{13}$$

Here, M_{Pi} and M_{Pl} are the pressure data point at x_{i} and at the plasma edge, respectively.

C. Internal topological constraint

Electron temperature measurements from TS and ECE also provide useful information on the internal magnetic surfaces that can be used to constrain the current profile [13,14]. In EFIT, these are included in the equilibrium reconstruction by incorporating their linearized responses into $\overline{\overline{R}}$ using the Picard iteration scheme based on magnetic information from the previous iteration similar to that used for the external flux loops as [14]

$$\sum_{\mathrm{i}}\left[G^{+}_{\mathrm{C_i}}\left(\bar{r}^{+}_{\mathrm{si}},\bar{r}_{\mathrm{ej}}\right)-G^{-}_{\mathrm{C_i}}\left(\bar{r}^{-}_{\mathrm{si}},\bar{r}_{\mathrm{ej}}\right)\right]I_{\mathrm{ej}}+\int_{\Omega^{\mathrm{m}}}dR'\,dZ'$$

$$\times\left[G^{+}_{\mathrm{C_i}}\left(\bar{r}^{+}_{\mathrm{si}},\bar{r}'\right)-G^{-}_{\mathrm{C_i}}\left(\bar{r}^{-}_{\mathrm{si}},\bar{r}'\right)\right]J_{\phi}\left[R',\psi^{\mathrm{m}}\left(\bar{r}',\bar{\alpha}^{\mathrm{m+1}}\right)\right]=0 \quad . \tag{14}$$

Here, + and – denote the i$^{\mathrm{th}}$ pair of data points from the TS and ECE measurements located at the outboard and the inboard side of the plasma, respectively, that have equal T_{e}.

IV. CHOICE OF BASIS FUNCTIONS AND BOUNDARY CONDITIONS

Proper choice of the basis functions and boundary conditions to represent the pressure and the current profiles is crucial to accurately reconstruct the equilibrium magnetic surfaces and current and pressure profiles. In EFIT, two choices of basis functions, polynomial or variable tension spline, can be used to represent the stream functions. The polynomial basis functions are

$$y_n(x) = x^n \quad . \tag{15}$$

The variable tension spline basis functions are expressed as [22]

$$y_n(x) = \frac{y_n''(x_n)}{\sigma_T^2}\left[\frac{\sinh(\sigma_T \Delta x_{n+1})}{\sinh(\sigma_T w_{n+1})} - \frac{\Delta x_{n+1}}{w_{n+1}}\right] + y_n(x_n)\frac{\Delta x_{n+1}}{w_{n+1}}$$

$$+ \frac{y_{n+1}''(x_{n+1})}{\sigma_T^2}\left[\frac{\sinh(\sigma_T \Delta x_n)}{\sinh(\sigma_T w_{n+1})} - \frac{\Delta x_n}{w_{n+1}}\right] + y_{n+1}(x_{n+1})\frac{\Delta x_n}{w_{n+1}} \quad , \quad x \in (x_n, x_{n+1}) \quad , \tag{16}$$

$$y_n(x) = 0 \quad , \quad x \notin (x_n, x_{n+1}) \quad .$$

Here, σ_T is the tension of the spline, $\Delta x_{n+1} = x_{n+1} - x$, $\Delta x_n = x - x_n$, $w_{n+1} = x_{n+1} - x_n$.

For reconstruction of plasma boundary and global current profile parameters such as I_p, β_p, and ℓ_i, the polynomial representation is usually sufficient. To reconstruct pressure and current profiles in plasmas with internal or edge transport barriers, a spline representation with knot points located near the transport barrier is needed. An option is available in EFIT to optimize the knot locations to best fit the pressure and MSE data using an external nonlinear optimization driver.

A representation is also available in EFIT to describe localized non-inductively driven current profiles such as those driven by electron cyclotron waves (ECCD) [20]

$$J_\phi(R,\psi) = J_{\phi 0}(R,\psi) + J_{local}(R,\psi) \quad , \tag{17}$$

$$J_{local} = \gamma_{local}\cos^2 k\tilde{x} \quad , \quad |\tilde{x}| \le 1 \quad , \tag{18}$$

$$J_{local} = 0 \quad , \quad |\tilde{x}| > 1 \quad .$$

Here, $J_{\phi 0}$ is a smooth background component represented using the polynomial basis functions, γ_{local} is the local current density amplitude, $k = \pi/2$, $\tilde{x} = (x - x_{\text{local}})/\Delta_{\text{local}}$, and x_{local} and Δ_{local} are the normalized poloidal flux at the local current density peak location and half width of the local current density channel, respectively. γ_{local} appears linearly and can be determined similarly as other current profile parameters from MSE and other internal current profile measurements. x_{local} and Δ_{local} appear nonlinearly and are determined in a separate external optimization loop [20].

A. Boundary conditions

In EFIT, the boundary conditions for $P'(\psi_1)$, $FF'(\psi_1)$, and $\Phi'_E(\psi_1)$ are conveniently implemented through the use of a boundary condition weighting vector

$$P'(\psi) = \sum_n \alpha_n y_n(x) - \alpha_p \sum_n \alpha_n y_n(1) \quad , \tag{19}$$

$$FF'(\psi) = \sum_n \gamma_n y_n(x) - \alpha_F \sum_n \gamma_n y_n(1) \quad , \tag{20}$$

$$\Phi'_E(\psi) = \sum_n \eta_n y_n(x) - \alpha_\Phi \sum_n \eta_n y_n(1) \quad . \tag{21}$$

Both zero and finite edge pressure gradient, current density, and electric field boundary conditions can be set by letting α_P, α_F, and $\alpha_\Phi = 1$ or 0. For Ohmic and L-mode plasmas, the zero edge boundary conditions are typically sufficient. For H-mode discharges, due to the large edge pressure gradient and the associated edge bootstrap and diamagnetic current density, finite edge boundary conditions are needed to accurately reconstruct the equilibrium. Forcing $P'(\psi_1)$, $FF'(\psi_1) = 0$ in H-mode configurations often lead to an inaccurate reconstruction of the plasma boundary.

A particularly useful parametrization and boundary condition for use with external magnetic reconstruction in both L- and H-mode discharges is the JT (J_ϕ Taylor) representation, where P' and FF' are represented using the polynomial basis functions and $P'(\psi_1)$ and $FF'(\psi_1)$ are only constrained to vanish weakly

$$P'(\psi) = \alpha_0 + \alpha_1 x \quad , \quad 0.1\alpha_0 + 0.1\alpha_1 = 0 \quad , \tag{22}$$

$$FF'(\psi) = \gamma_0 + \gamma_1 x + \gamma_2 x^2 \quad , \quad 0.1\gamma_0 + 0.1\gamma_1 + 0.1\gamma_2 = 0 \quad , \tag{23}$$

The additional freedom gained by allowing $P'(\psi_1)$, $FF'(\psi_1)$ to have a finite values through these constraints is sufficient to allow accurate reconstruction of the plasma boundary. There are five parameters. Three of them describe β_p, ℓ_i, and I_p, and the remaining two are determined by the two boundary conditions on $P'(\psi_1)$ and $FF'(\psi_1)$ as given in Eqs. (22) and (23). Note that these two boundary constraints are solved together with all other magnetic measurements as part of the response matrix $\overline{\overline{R}}$. At each iteration, the linear minimization problem is solved using the singular value decomposition method by decomposing $\overline{\overline{R}}$ into a diagonal matrix. The coefficients 0.1 appearing in these constraint equations describe the weak weighting of these constraints relative to the other magnetic measurements when $\overline{\overline{R}}$ is decomposed. The reconstructed plasma boundary, β_p, ℓ_i, and I_p are not sensitive to the exact values of the coefficients chosen. Increasing the coefficients from 0.1 to 0.2 only changes the results slightly.

B. Illustrative examples

In this Section, various reconstruction examples using external magnetic, MSE, and kinetic profile data are given to illustrate equilibrium reconstructions in DIII-D. To fully reconstruct the equilibrium pressure and current profiles and the associated magnetic topology self-consistently, MSE and kinetic profile data must be used in conjunction with external magnetic data. This is illustrated in Fig. 2, where a fully reconstructed equilibrium of a DIII-D H-mode divertor discharge using 39 flux loops, 55 magnetic probes, 1 full Rogowski loop, 34 channels of MSE measurements, and kinetic profile data from TS, ECE, and CER is shown. The reconstruction is done using 3-knot spline representations for P' and FF', and a two-term polynomial representation for Φ'_E. A 129×129 (129 grid points in the R direction and 129 grid points in the Z direction) version of EFIT is used with a relative equilibrium convergence error of $\varepsilon = Max\left|\left(\psi^{m+1} - \psi^{m}\right) \Big/ \left(\psi_0^{m+1} - \psi_1^{m+1}\right)\right| \sim 10^{-8}$. Shown in Fig. 3 are the measured and fitted T_i, T_e, and n_e profiles and the computed P_f profile used to form the total P, the measured and fitted P and MSE B_z profiles, the reconstructed magnetic surfaces, flux surface average $\langle J_\phi \rangle$, q, and E_R profiles. The reconstructed equilibrium fits all the magnetic, MSE, and kinetic data well. Also shown is the E_R profile (dotted curve) obtained from CER measurement of carbon impurity, which agrees well with the reconstructed E_R (solid curve).

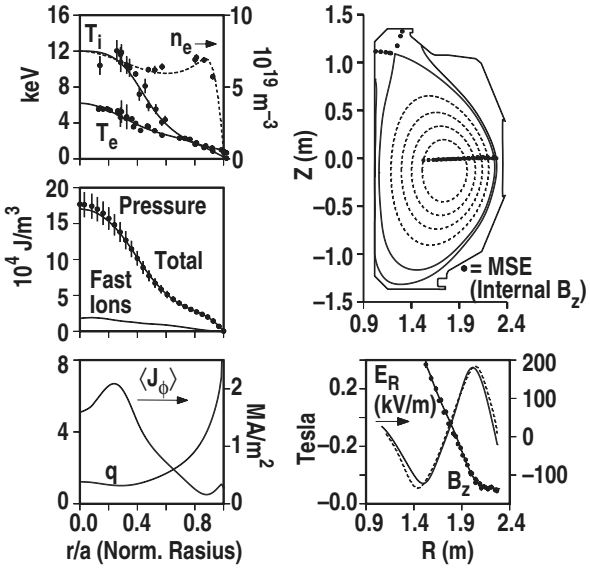

Fig. 2. Measured (symbols) and fitted (curves) temperature and density profiles and the computed fast ion pressure P_f used to form P, measured (symbols) and fitted (curves) P and MSE B_z profiles, reconstructed magnetic surfaces, q, and flux surface average $\langle J_\phi \rangle$ profiles, reconstructed E_R (solid curve) and E_R from CER measurement of carbon impurity (dashed curve) for DIII-D H-mode divertor discharge 92043 at 2200 ms.

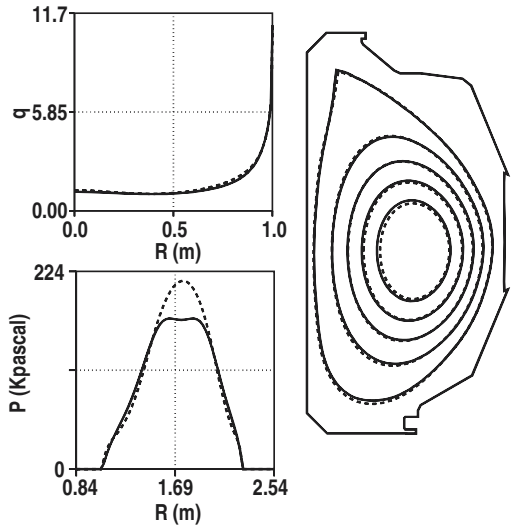

Fig. 3. Comparison of magnetic surfaces, the q profile, and the pressure profile along the midplane reconstructed using external magnetic and MSE measurements (solid curves) against those reconstructed fully using kinetic, MSE, and external magnetic data (dashed curves) for DIII-D H-mode divertor discharge 92043 at 2200 ms.

Equilibrium reconstruction using external magnetic data alone can accurately yield plasma shape, global pressure, and current profile parameters only. This is illustrated in Fig. 4 and Table I, where the magnetic surfaces, P and q profiles, and various pressure and current profile

parameters reconstructed magnetically using 39 flux loops, 55 magnetic probes, and 1 full Rogowski loop data are compared to those from the full reconstruction case using MSE, kinetic, and external magnetic data discussed above. The magnetic reconstruction is carried out using the JT representation for P' and FF'. A 65×65 version of EFIT is used with $\varepsilon \sim 10^{-4}$. The reconstructed plasma shape and global plasma pressure and current profile parameters from magnetic reconstruction agree well with those from full reconstruction. As expected, reconstruction using external magnetic data does not provide accurate information on the P and q profiles. q_0 and the minimum q value, $q_{\min}$, from the magnetically reconstructed case are both 0.76, whereas the values from the full reconstruction case are 1.23 and 1.01. The pressure profile from the full reconstruction case has a clear edge pedestal, as expected for H-mode plasma, whereas this is absent in the magnetically reconstructed case.

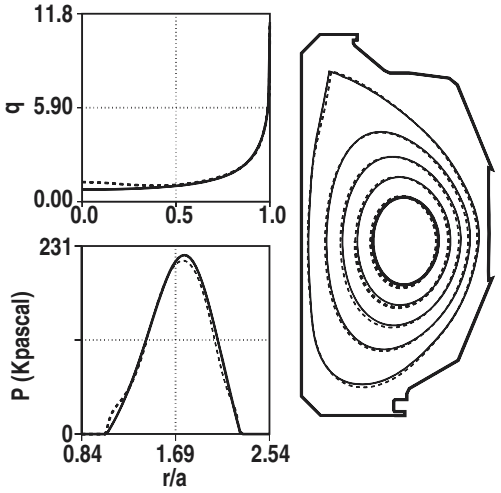

Fig. 4. Comparison of magnetic surfaces, the q profile, and the pressure profile along the midplane reconstructed using only external magnetic measurements (solid curves) against those reconstructed fully using internal kinetic, MSE, and external magnetic data (dashed curves) for DIII-D H-mode divertor discharge 92043 at 2200 ms.

Equilibrium reconstruction using MSE together with external magnetic data can accurately yield plasma shape, global pressure and current profile parameters, as well as the q profile. This is illustrated in Fig. 3 and Table I, where the magnetic surfaces, P and q profiles, and various pressure and current profile parameters reconstructed using 39 flux loops, 55 magnetic probes, and 1 full Rogowski loop data, and 34 channels of MSE measurements are compared to those from the full reconstruction case using MSE, kinetic, and external magnetic data discussed

above. The reconstruction is carried out using 2- and 3-knot spline representation for P' and FF' and a two-term polynomial representation for Φ'_E. A 65×65 version of EFIT is used with $\varepsilon \sim 10^{-4}$. The reconstructed plasma shape, q profile, global plasma pressure, and current profile parameters agree well with those from the full reconstruction case. As expected, reconstruction using MSE only does not provide an accurate P profile. q_0 and $q_{\min}$ for this case are 1.13 and 1.00. The value of $q_0 \sim 1.13$ is slightly lower compared with the value of 1.23 from the case with kinetic profile. The reconstructed E_R profile (not shown) also agrees well with that from the full reconstruction case.

Table I: Comparison of Plasma Shape, Pressure, and Current Profile Parameters for Four DIII-D Reconstructions Using External Magnetic, External Magnetic and MSE, External Magnetic and MSE plus Kinetic Data, External Magnetic and MSE plus Kinetic and Rotation Data for Shot 92043 at 2200 ms,

Case	Magnetic	Magnetic + MSE	Magnetic + MSE + Kinetic	Magnetic + MSE + Kinetic + Rotation
Grid Size	65×65	65×65	129×129	129×129
I_p (MA)	1.482	1.481	1.486	1.492
$\Omega\ (m^3)$	19.87	19.74	19.85	19.85
R_G (m)	1.675	1.669	1.666	1.667
Z_G (m)	-0.028	-0.025	-0.038	-0.037
a (m)	0.608	0.604	0.604	0.604
κ	1.84	1.86	1.87	1.87
δ_U	0.76	0.75	0.72	0.73
δ_L	0.37	0.36	0.36	0.36
R_M (m)	1.770	1.744	1.758	1.762
Z_M (m)	-0.121	-0.126	-0.130	-0.129
κ_M	1.31	1.40	1.43	1.45
q_0	0.76	1.13	1.23	1.32
$q_{\min}$	0.76	1.00	1.01	1.00
q_{95}	4.73	4.79	4.77	4.78
β_N	3.54	3.56	3.49	3.37
β_p	1.63	1.65	1.62	1.56
β_T (%)	4.08	4.10	4.03	3.90
ℓ_i	1.14	1.21	1.16	1.14
W_p (kJ)	2169	2183	2164	2096
W_ω (kJ)	0	0	0	86.6

V. EQUILIBRIUM RECONSTRUCTION WITH ROTATION

Equilibrium reconstruction with rotation was first implemented into EFIT in 1994 as part of an effort to investigate the effects of rotation and radial electric field on the MSE measurements [19]. For an axisymmetric toroidal system, in the presence of toroidal rotation the equilibrium equation can be written as [18]

$$\Delta^* \psi = -\mu_0 R J_\phi \quad , \; J_\phi = R\frac{\partial P(R,\psi)}{\partial \psi} + \frac{\mu_0 F F'(\psi)}{4\pi^2 R} \quad , \tag{24}$$

$$\frac{\partial P(R,\psi)}{\partial R} = R\rho_m(R,\psi)\omega_\phi^2(\psi) \quad . \tag{25}$$

Here, ρ_m is the plasma mass density and ω_ϕ is the plasma toroidal rotation frequency. In the presence of toroidal flow, P is no longer constant on a magnetic surface due to the centrifugal force, and the equilibrium is constrained by two coupled partial differential equations describing force balance in the directions normal and tangential to a magnetic surface.

For an ideal plasma consisting of electrons, ions, and a single impurity species with a flat Z_{eff} and T_i and T_e constant on a magnetic surface, $P(R,\psi) = \left[n_i(R,\psi) + n_z(R,\psi)\right] T_i(\psi) + n_e(R,\psi) T_e(\psi)$ and Eq. (25) can be integrated analytically to yield

$$P(R,\psi) = P_0(\psi)\exp\left[\frac{P_\omega(\psi)}{P_0(\psi)}\frac{\left(R^2 - R_0^2\right)}{R_0^2}\right] \quad , \quad P_0(\psi) = 2n_{e0}(\psi)\, T(\psi) \quad , \tag{26}$$

$$P_\omega(\psi) = R_0^2\, \rho_{m0}(\psi)\, \omega_\phi^2(\psi)/2 \quad , \quad \rho_{m0}(\psi) = n_{e0}(\psi)\, m_m \quad . \tag{27}$$

Here, R_0 is a reference major radius, and $n_{e0}(\psi) = n_e(R_0,\psi)$. T and m_m are the plasma equivalent temperature and mass

$$P(R,\psi) = 2n_e(R,\psi)\, T(\psi) \quad , \quad 2T(\psi) = T_e(\psi) + \frac{T_i(\psi)}{Z_i}\left[1 - \frac{(Z_{eff} - Z_i)}{Z_z}\right] \quad , \tag{28}$$

$$\rho_m(R,\psi) = n_e(R,\psi)\, m_m \quad , \quad m_m = \frac{m_i}{Z_i}\left[1 + \frac{(Z_{eff} - Z_i)}{(Z_z - Z_i)}\left(\frac{m_z Z_i}{m_i Z_z} - 1\right)\right] \quad . \tag{29}$$

A_i, A_z, m_i, and m_z are the atomic numbers and mass of the main ion and impurity, respectively. The pressure-driven term in J_ϕ can then be conveniently written in terms of $P_0(\psi)$ and $P_\omega(\psi)$ as

$$J_\phi^P(R,\psi) = \frac{\partial P(R,\psi)}{\partial \psi} = P_0'(\psi)\,\frac{P}{P_0}\left(1 - \frac{P_\omega}{P_0}\,\frac{R^2 - R_0^2}{R_0^2}\right) + P_\omega'(\psi)\,\frac{P}{P_0}\,\frac{\left(R^2 - R_0^2\right)}{R_0^2} \quad . \tag{30}$$

The analytic integration significantly reduces the complexity of the problem. When the rotational energy is small, $\rho_m R^2 \omega_\phi^2 \sim O(1/A)$ where $A = R_m/a$ is the plasma aspect ratio, Eq. (25) can also be integrated analytically to yield

$$P(R,\psi) = P_0(\psi) + P_\omega(\psi)\left(\frac{R^2 - R_0^2}{R_0^2}\right) \quad . \tag{31}$$

As can be seen from Eqs. (26) and (31), to reconstruct the equilibrium with rotation, three stream functions $P_0(\psi)$, $P_\omega(\psi)$, and $FF'(\psi)$ are needed. As in the case without rotation, the equilibrium is reconstructed by parametrizing these three stream functions using the basis functions y_n in terms of the linear parameters, α_n and γ_n, and ω_n as

$$P_0'(\psi) = \sum_n \alpha_n y_n(x) \quad , \quad FF'(\psi) = \sum_n \gamma_n y_n(x) \quad . \quad P_\omega'(\psi) = \sum_n \omega_n y_n(x) \quad . \tag{32}$$

The optimization problem is then solved by linearizing the responses due to the rotational terms using Eqs. (30) and (31) and incorporating them into the response matrix $\overline{\overline{R}}$ [19]

$$J_\phi^{P(m+1)} = P_0'\left(\psi^m, \overline{\alpha}^{m+1}\right)\left[\frac{P}{P_0}\left(1 - \frac{P_\omega}{P_0}\,\frac{R^2 - R_0^2}{R_0^2}\right)\right]^m + P_\omega'\left(\psi^m, \overline{\alpha}^{m+1}\right)\left[\frac{P}{P_0}\,\frac{R^2 - R_0^2}{R_0^2}\right]^m \quad . \tag{33}$$

To reconstruct the equilibrium with rotation, additional plasma mass density and toroidal rotation profile data, ρ_{m0} and ω_ϕ, are needed. An example of DIII-D equilibrium reconstruction with toroidal rotation is given in Table I and Fig. 5, where various plasma pressure and current profile parameters and the reconstructed magnetic surfaces, the q profile and P profile along the midplane reconstructed using magnetic, MSE, kinetic, and rotation profile data are compared to

those from the kinetic reconstruction case without rotation given in Fig. 2. Also shown in Fig. 5 is the fitted P_ω profile that agrees well with the measured P_ω profile formed from ρ_{m0} and ω_ϕ. The reconstruction is carried out using three-knot spline representations for P_0' and FF' and two- and three-term polynomial representations for Φ_E' and P_ω with a 129×129 version of EFIT. As shown in Fig. 5 and Table I, in this case the rotation energy is small, $W_\omega \sim 4\,\%$ of the total plasma stored energy W_p, The effects of toroidal rotation on the equilibrium are small. The reconstructed magnetic surfaces, P and q profiles are barely distinguishable from those reconstructed without rotation. W_p is slightly lower and q_0 is slightly higher compared with the no rotation case.

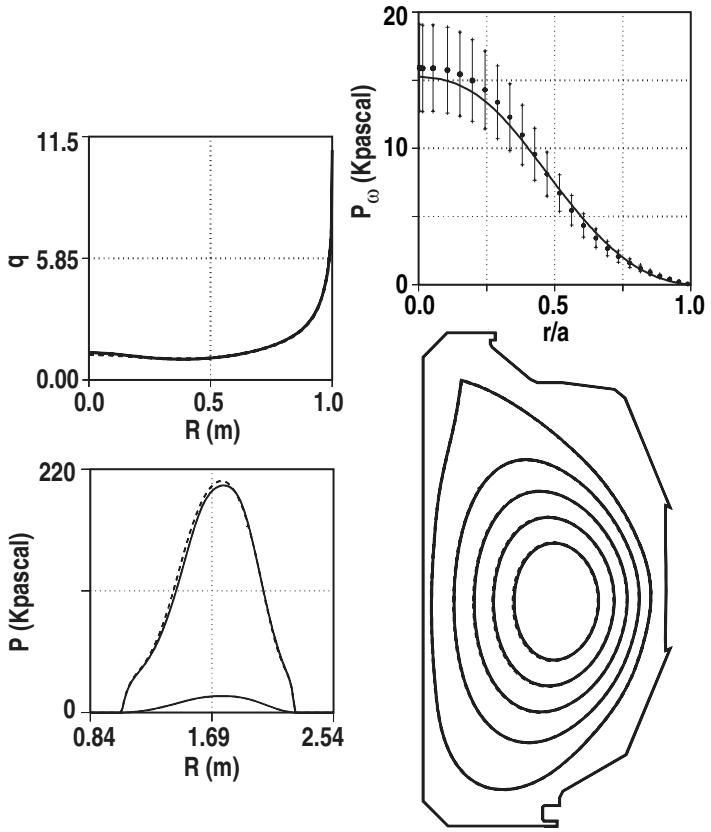

Fig. 5. Comparison of magnetic surfaces, the q profile, and the pressure profile along the midplane reconstructed using toroidal rotation, kinetic, MSE and external magnetic measurements (solid curves) against those reconstructed without rotation data (dashed curves) for DIII-D H-mode divertor discharge 92043 at 2200 ms. Also shown are the reconstructed (solid curve) and measured (symbols) rotation pressure profile P_ω for the reconstruction case with rotation.

VI. EQUILIBRIUM RECONSTRUCTION APPLICATIONS AND SUMMARY

Since its inception nearly 20 years ago, EFIT has grown to become a major analysis tool used in many tokamak laboratories and fusion research institutions worldwide [13,23–30]. As described in the previous sections, over the years many improvements and developments have been made to EFIT. These include the implementation of spline and local representations, a halo current model to reconstruct equilibrium during VDE, reconstruction using internal current and kinetic profile measurements, reconstruction using internal magnetic topological constraint, and reconstruction with toroidal plasma rotation. Many of the reconstruction algorithms that have been successfully developed and used in EFIT have also been employed in the DIII-D real time EFIT plasma control system, rtEFIT [5]. Detailed documentation and latest developments of EFIT can be found in the EFIT web site http://web.gat.com/efit.

One of the main EFIT applications is to provide between-shot equilibrium analysis to support plasma operation. In DIII-D, typically 250 time slices of equilibrium reconstruction using external magnetic data and 150 time slices of reconstruction using magnetic and MSE data are analyzed between plasma shots during experimental operations on a 12-node dual CPU Linux cluster running at 2.66 GHz [31]. An EFIT grid size of 65×65 is used. The entire 250 magnetic reconstructions are distributed uniformly over the 12 nodes and take approximately 25 s that includes 6 s to retrieve the magnetic data. The 150 reconstructions with MSE and magnetic data take approximately 35 s that includes 6 sec to retrieve the magnetic data and 15 s to retrieve and process the MSE data. Future plans include adding full kinetic equilibrium reconstructions to the between-shot analysis.

A second major application of EFIT is to provide magnetically reconstructed plasma global confinement and pressure data for confinement and stability scaling studies [32–36]. A third major EFIT application is the full reconstruction of MHD equilibria using internal current and kinetic profile data for detailed stability analysis [37]. For DIII-D stability analysis, a large 129×129 grid EFIT that is tightly converged to $\varepsilon < 10^{-8}$ is typically used. A fourth major DIII-D

EFIT application is the determination of the non-inductive current profiles from a series of time-dependent EFIT equilibrium reconstructions using MSE data [38]. For highly localized ECCD in DIII-D, to accurately reconstruct the current profile it is necessary to use the local representation given in Eqs. (17) through (18) [20].

For next-step burning plasma experiments such as ITER, the external coils are located outside of the toroidal magnetic field coils and far away from the plasma. Thus, accurate equilibrium reconstruction and plasma control in these devices become more challenging than that in existing devices such as DIII-D, which has external coils located close to the plasma. It is important in the design of the magnetic and internal current profile diagnostics for equilibrium reconstruction in these devices to take into account the physics issues discussed here. The presence of ferromagnetic inserts will increase the complexity of magnetic reconstruction in ITER. The techniques previously developed to handle the iron core in the JET tokamak for magnetic reconstruction using EFIT [23] can potentially be extended to treat the ferromagnetic inserts in ITER. More magnetic diagnostics will be needed for determination of the magnetization current in the ferromagnetic material crucial for accurate magnetic reconstruction.

REFERENCES

[1] J.L. Luxon, B.B. Brown, Nucl. Fusion **22**, 813 (1982).

[2] L.L. Lao, *et al.,* Nucl. Fusion **25**, 1421 (1985).

[3] L.L. Lao, *et al.,* Nucl. Fusion **25**, 1611 (1985).

[4] D.W. Swain, G.H. Neilson, Nucl. Fusion **22**, 1015 (1982).

[5] J.R. Ferron, *et al.,* Nucl. Fusion **38**, 1055 (1998).

[6] B.J. Braams, Plasma Phys. Contr. Fusion **33**, 715 (1991).

[7] J.P. Freidberg, *et al.,* Plasma Phys. Contr. Fusion **35**, 1641 (1993).

[8] V.D. Pustovitov, Nucl. Fusion **41**, 721 (2001).

[9] F.M. Levinton, *et al.,* Phys. Rev. Lett. **63**, 2060 (1989).

[10] D. Wroblewski, L.L. Lao, Rev. Sci. Instrum. **63**, 5140 (1992).

[11] B.W. Rice, Fusion Eng. Design **37**, 517 (1997).

[12] L.L. Lao, *et al.,* Nucl. Fusion **30**, 1035 (1990).

[13] L.C. Appel, *et al.,* Nucl. Fusion **41**, 169 (2001).

[14] C. Zhang, L.L. Lao, General Atomics Report GA-A24583, to be submitted to Nucl. Fusion.

[15] B.W. Rice, *et al.,* Nucl. Fusion **37**, 517 (1997).

[16] B.W. Rice, *et al.,* Phys. Rev. Lett. **79**, 2694 (1997).

[17] D.M. Thomas, Rev. Sci. Instrum. **74**, 1541 (2003).

[18] H.R. Strauss, Phys. Fluids **16**, 1377 (1973).

[19] L.L. Lao, *et al.,* Bull. Am, Phys. Soc. **39**, 1580 (1994).

[20] L.L. Lao, *et al.,* AIP Proc. of the 14th Top. Conf. in Radio Frequency Power in Plasmas **595**, 310 (2001).

[21] L.L. Lao, T.H. Jensen, Nucl. Fusion **31**, 1909 (1991).

[22] A.K. Cline, Commun. ACM **17**, 218 (1974).

[23] D.P. O'Brien, *et al.,* Nucl. Fusion **32**, 1351 (1992).

[24] B. Nelson, *et al.,* Phys. Rev. Lett. **72**, 3666 (1994).

[25] B. Lee, N. Pomphrey, Fusion Tech. **36**, 278 (1999).

[26] Y. In, *et al.,* Nucl. Fusion **40**, 1463 (2000).

[27] T. Oikawa, *et al.,* Nucl. Fusion **40**, 435 (2000).

[28] S.A. Sabbagh, *et al.,* Nucl. Fusion **41**, 1601 (2001).

[29] W. Zwingmann, Nucl. Fusion **43**, 842 (2003).

[30] J. Li, *et al.,* Phys. Plasmas **10**, 1653 (2003).

[31] Q. Peng, *et al.,* Fusion Eng. Design **60**, 319 (2002).

[32] E.J. Strait, Phys. Plasmas **1**, 1415 (1994).

[33] M. Greenwald, *et al.,* Phys. Plasmas **2**, 2308 (1995).

[34] A. Sykes, *et al.,* Nucl. Fusion **39**, 1271 (1999).

[35] S.M. Kaye, *et al.,* Phys. Plasmas **8**, 1977 (2001).

[36] S.A. Sabbagh, *et al.,* Phys. Plasmas **9**, 2085 (2002).

[37] A.D. Turnbulll, *et al.,* Nucl. Fusion **42**, 917 (2002).

[38] C.B. Forest, *et al.,* Phys. Rev. Lett. **73**, 2444 (1994).

ACKNOWLEDGMENTS

The work discussed in this paper was supported by U.S. Department of Energy under DE-FC02-04ER54698 and W-7405-ENTG-48.

This paper summarizes the work done by the DIII-D program in this area over the past twenty years or more and includes the contributions of many members of the DIII-D Team listed in the Appendix of this volume of Fusion Science and Technology.

THE DIII-D TEAM (1986-2005)
AND THEIR AFFILIATIONS

[The number following each name corresponds to the affiliation shown on page 3 of this Appendix.]

Abla,	G.	1
Allais,	F.	55
Allen,	S. L.	4
Anderson,	P. M.	1
Andre,	R.	8
Antar,	G.	33
Antoniuk,	N.	33
Astapkovich,	A.	60
Attenberger,	S.	5
Austin,	M. E.	37
Baggest,	D. S.	1
Baity,	F. W.	5
Bakalarski,	J. P.	1
Baker,	D. R.	1
Baldwin,	D. E.	1
Barber,	D. E. G.	5
Bastasz,	R.	9
Baxi,	C. B.	1
Baylor,	L. R.	5
Becoulet,	M.	44
Bernabei,	S.	8
Bialek,	J. M.	21
Biglari,	H.	33
Boedo,	J. A.	33
Bogatu,	I. N.	1
Boivin,	R. L.	1
Bondeson,	A.	40
Bozek,	A. S.	1
Bramson,	G.	1
Bravenec,	R. V.	37
Bray,	B. D.	1
Brennan,	D. P.	1
Brezinski,	S.	48
Brizard,	A.	9
Broesch,	J. D.	1
Brooks,	N. H.	1
Brown,	B.	1
Brown,	R.	1
Buchenauer,	D.	9
Budny,	R. V.	8
Burley,	B.	1
Burrell,	K. H.	1
Burruss,	J. R.	1
Buttery,	R. J.	53
Buzhinskij,	O.	64
Callen,	J. D.	39
Callis,	R. W.	1
Campbell,	G. L.	1
Campo,	C. S.	1
Candy,	J. M.	1
Carlstrom,	T. N.	1
Carolipio,	E.	31
Carreras,	B.	5
Cary,	W. P.	1
Casper,	T. A.	4
Cecil,	E.	20
Challis,	C. D.	53
Chan,	V. S.	1
Chance,	M. S.	8
Chang,	Z.	39
Chen,	L.	65
Chenglum,	Y.	67
Chin,	E.	1
Chiu,	H. K.	1
Chiu,	S. C.	1
Choi,	M.	1
Chu,	M. S.	1
Cirant,	S.	50
Coda,	S.	27
Colchin,	R. J.	5
Colleraine,	A. P.	1
Combs,	S. K.	5
Comer,	K.	39
Content,	D.	24
Culver,	J.	71
Cummings,	J. W.	1
Cuthbertson,	J. W.	33
Davis,	J. W.	71
Davis,	L.	1
Davis,	W.	8
DeBoo,	J. C.	1
DeGentile,	J. C.	44
deGrassie,	J. S.	1
DeHaas,	J.	4
Delaware,	S.	1
Deranian,	R. D.	1
Diamond,	P. H.	33
Diao,	G.	56
DiMartino,	M.	1
Doan,	K. H.	1
Doane,	J. L.	1
Doerner,	R. P.	33
Doi,	I.	72
Dokouka,	V.	64
Dominguez,	R. R.	1
Dorland,	W.	35
Dorris,	J.	27
Doyle,	E. J.	32
Duong,	H.	31
Edgell,	D. H.	26
Ejima,	S.	1
Ejiri,	A.	58
Ellis,	R. A. III	8
Ellis,	R. F.	35
Ernst,	D.	8
Estrada-Mila,	C.	33
Evanko,	R. G.	1
Evans,	T. E.	1
Feder,	R.	8
Feibush,	E.	8
Fenstermacher,	M. E.	4
Fenzi,	C.	39
Ferguson,	W.	4
Ferron,	J. R.	1
Finken,	K. H.	48
Finkenthal,	D. K.	28
Fisher,	R. K.	1
Fitzpatrick,	J.	31
Fitzpatrick,	R.	37
Flanagan,	S. M.	1
Fonck,	R. J.	39
Forest,	C. B.	1
Fowler,	T. K.	30
Fransson,	C-M.	19
Fredd,	E.	8
Fredrickson,	E.	8
Freeman,	J.	1
Freeman,	R. L.	1
Friend,	M. E.	1
Fuchs,	C.	52
Fukuda,	T.	56
Fukumoto,	H.	14
Futch,	A. H.	4
Fyaretdinov,	A.	62
Gafert,	J.	52
Galkin,	S. A.	61
Gallix,	R.	1
Garofalo,	A. M.	21
Garstka,	G.	35
Gentle,	K. W.	37
Ghendrih,	Ph.	44
Gianakon,	T.	39
Gianella,	R.	44
Gilleland	J. R.	1
Gilmore,	M.	36
Giruzzi,	G.	44
Glad,	T.	1
Glasser,	A. H.	3
Gohil,	P.	1
Gootgeld,	A. A.	1
Gorelov,	I. A.	1
Goulding,	R. H.	5
Grantham,	F.	1
Gray,	D. S.	33
Graznevitch,	M.	53
Green,	M. T.	1
Greene,	J. M.	1
Greene,	K. L.	1
Greenfield,	C. M.	1
Greenough,	N. L.	8
Groebner,	R. J.	1
Groth,	M.	4
Grunloh,	H. J.	1
Gryaznevich,	M.	53
Günter,	S.	52
Guo,	S. C.	41
Gupta,	D.	39
Haas,	G.	52
Hahm,	T. S.	8
Hanai,	S.	14
Hansink,	M. J.	1
Harrington,	R. J.	29
Harris,	J. H.	69
Harris,	T. E.	1
Harvey,	R. W.	12
Haskovec,	J.	1
Hatae,	T.	56
Hatcher,	R.	8
Hawkes,	N. C.	53
Hayden,	D.	34
Heckman,	E.	1
Hegna,	C. C.	39
Heiberger,	M.	1
Heidbrink,	W. W.	31
Helton,	F. J.	1
Hender,	T. C.	53
Henkel,	G.	5
Henline,	P. A.	1
Hill,	D. N.	4
Hillis,	D. L.	5
Hinton,	F. L.	1
Hobirk,	J.	52
Hodapp,	T. R.	1
Hoffman,	D. J.	5
Hoffmann,	E. H.	1
Hogan,	J. T.	5
Holcomb,	C.	4
Holland,	C.	33
Hollerbach,	M. A.	1
Hollman,	E. M.	33
Holtrop,	K. L.	1
Hong,	R. -M.	1
Hosea,	J. C.	8
Hosogane,	N.	56
Houlberg,	W. A.	5
Howald,	A. M.	1
Howard,	N.	34
Howell,	D. F.	53
Howl,	W.	1
Hsieh,	C. -L.	1
Hsu,	W. L.	9
Humphreys,	D. A.	1
Hyatt,	A. W.	1
Ikezi,	H.	1
Imbeaux,	F.	44
In,	Y.	13
Indireshkumar,	K.	8
Isayama,	A.	56
Isler,	R. C.	5
Ivanov,	A.	61
Jackson,	G. L.	1
Jacques,	A. M.	1
Jaeger,	F.	5
Jahns,	G. L.	1
Jakubowski,	M.	39
Jalufka,	N. W.	23
James,	R. A.	4
Janeschitz,	G.	52
Janz,	S.	35
Jarboe,	T.	38
Jardin,	S. C.	8
Jayakumar,	R. J.	4
Jensen,	T. H.	1
Jernigan,	T. C.	5
Joffrin,	E. H.	44
Johnson,	E.	1
Johnson,	L. C.	8
Johnson,	R. D.	1
Jong,	R.	4
Junge,	R.	1
Kajiwara,	K.	6
Kamada,	Y.	56
Kaplan,	D. H.	1
Katsuro-Hopkin	O.	21
Kawano,	Y.	56
Keith,	K. M.	1
Kellman,	A. G.	1
Kellman,	D. H.	1
Kempenaars,	M. A. H.	49
Kessel,	C.	8
Khayrutdinov,	R.	64
Kim,	C.	39
Kim,	J. S.	13
Kim,	J.	1
Kim,	K. W.	32
Kim,	Y.	1
Kinoshita,	S.	14
Kinsey,	J. E.	25
Kirkpatrick,	N. P.	1
Klepper,	C. C.	5
Kohli,	J.	1
Konings,	J. A.	49
Konoshima,	S.	56
Kramer,	G. J.	8
Krasheninnikov,	S. I.	33
Krasilnikov,	A.	64
Kruger,	S. E.	18
Kubo,	H.	56
Kupfer,	K.	7
Kurki-Suonio,	T.	30
La Haye,	R. J.	1
Labik,	G.	8
Lao,	L. L.	1
Lasnier,	C. J.	4
Latchem,	J. W.	1
Laughon,	G. J.	1
Lazarus,	E. A.	5
Lebedev,	V.	33
Leboeuf,	J. -N	32
Lee,	B.	32
Lee,	H.	66
Lee,	J. -H.	32
Lee,	J.	31
Lee,	P.	1
Lee,	R. L.	1
Legg,	R. A.	1
Lehecka,	T.	32
Lehmer,	R.	33

THE DIII-D TEAM (1986-2005) (continued)
AND THEIR AFFILIATIONS

[The number following each name corresponds to the affiliation shown on page 3 of this Appendix.]

Leikind, B. 1
Leonard, A. W. 1
Leuer, J. A. 1
Lightner S. 1
Lin-Liu, Y. R. 68
Lippmann, S. I. 1
Lisgo, S. 71
Lister J. 43
Liu, C. 1
Liu, Y. Q. 40
Lloyd, B. 53
Loarte, A. 52
Lodestro, L. L. 4
Lohr, J. M. 1
Lomas, P. J. 51
Lowry, C. 51
Lu, G. 1
Luce, T. C. 1
Luckhardt, S. C. 33
Ludescher-Furth C. 8
Luhmann, N. C. Jr. 32
Lukash, V. 64
Luo, Y. 31
Luxon, J. L. 1
Mahdavi, M. A. 1
Mailloux, J. 53
Maingi, R. 5
Makariou, C. C. 1
Makowski, M. A. 4
Mandrekas, J. 22
Manickam, J. 8
Manini, A. 52
Maraschek, M. E. 52
Martin, Y. 43
Matsuda, K. 1
Matsumoto, H. 56
Matthews, G. 53
Mauel, M. E. 21
Mauzey, P. S. 1
Mayberry, M. 1
Mazon, D. 44
McChesney, J. M. 1
McCune, D. C. 8
McHarg, B. B. 1
McKee, G. R. 39
McKelvey, T. 1
McLean, A. G. 71
Menard, J. E. 8
Menon, M. M. 5
Messiaen, A. M. 46
Mett, R. 1
Meyer, W. H. 4
Middaugh, K. R. 1
Mikkelsen, D. 8
Miller, R. L. 1
Miller, S. M. 1
Mills, B. 9
Minor, D. H. 1
Mioduszewski, P. K. 5
Mizuuchi, T. 59
Moeller, C. P. 1
Moller, J. M. 4
Monier-Garbet P 44
Moore, D. 1
Mossessian, D. 27
Moyer, R. A. 33
Mui, A. 28
Murakami, M. 5
Nagy, A. 8
Nave, M. F. A. 47
Navratil, G. A. 21
Nazikian, R. 8
Nerem, A. 1
Nevins, W. M. 4
Neyatani, Y. 56
Nikolski, Y. 1
Nilsen, M. P. 1
Nilson, D. E. 4
Nissley, L. E. 1
Noll, P. 51
Ohkawa, T. 1
Ohyabu, N. 58
Oikawa, T. 56
Okabayashi, M. 8
Okazaki, T. 56
Olstad, R. A. 1
Omelchenko, Y. 1
O'Neill, R. C. 1
Ongena, J. 46
Opimach, I. 62
Osborne, T. H. 1
Overskei, D. O. 1
Owens, L. W. 5
Ozeki, T. 56
Parker, C. T. 1
Parks, P. B. 1
Parsell, R. 8
Patterson, R. 1
Pawley, C. J. 1
Pearlstein, L. D. 4
Peavy, J. J. 1
Peebles, W. A. 32
Penaflor, B. G. 1
Peng, Q. 1
Perkins, F. W. 8
Perry, M. 24
Petersen, P. I. 1
Petrach, P. M. 1
Petrie, T. W. 1
Petty, C. C. 1
Pham, N. Q. 1
Phelps, D. A. 1
Phelps, R. D. 1
Phelps, W. 1
Philipona, R. 32
Phillips, J. C. 1
Pigarov, A. Yu. 33
Piglowski, D. A. 1
Pinches, S. D. 52
Pinsker, R. I. 1
Pletzer, A. 8
Politzer, P. A. 1
Ponce, D. 1
Porkolab, M. 27
Porter, G. D. 4
Prater, R. 1
Pretty, D. G. 69
Pronko, S. G. 1
Puhn, F. 1
Punjabi, A. 23
Raftopopulos, S. 8
Ramsey, A. 8
Randerson, L. E. 8
Rasmussen, D. A. 5
Rawls, J. 1
Redler, K. 1
Reiman, A. 8
Reimerdes, H. 21
Reis, E. E. Jr. 1
Remsen, D. B Jr. 1
Ren, C. 39
Rensink, M. E. 4
Rettig, C. L. 32
Rewoldt, G. 8
Rhodes, T. L. 32
Rice, B. W. 4
Riedy, P. 1
Robinson, J. I. 1
Rock, P. 1
Rodriguez, J. 34
Rogers, J. 8
Rognlien, T. D. 4
Rolens, G. 1
Rosenbluth, M. N. 1
Ross, D. W. 37
Rost, J. C. 27
Rothwell, D. A. 1
Rudakov, D. L. 33
Ruskov, E. 31
Ryter, F. 52
Sabbagh, S. 21
Sager, G. T. 1
Saibene, G. 52
Saigusa, M. 56
Sakurai, S. 56
Sauter, O. 43
Sauthoff, N. 8
Savercool, R. I. 1
Savrukhin, P. 62
Schachter J. M. 1
Schaffer, M. J. 1
Schaubel, K. M. 1
Schissel, D. P. 1
Schlossberg, D. J. 39
Schmidt, G. 8
Schmitz, L. 32
Schnack, D. D. 17
Schuster, E. 25
Scoville, J. T. 1
Sellers, D. 1
Semenets, Y. 64
Seraydarian, R. P. 1
Sevier, D. L. 1
Shafer, M. W. 39
Shapiro, M. 27
Shimada, M. 56
Shoji, T. 56
Shoolbred, K. C. 1
Simonen, T. C. 1
Sips, A. C. C. 52
Skinner, S. M. 1
Sleaford, B. 1
Smirnov, A. P. 63
Smith, J. P. 1
Smith, P. 1
Smith, T. L. 1
Snider, R. T. 1
Snyder, P. B. 1
Solano, E. R. 45
Söldner, F. 51
Solomon, W. M. 8
Soon, E. 33
Squire, J. 6
Srivivasan, M. 32
St John, H. E. 1
Stacey, W. M. 22
Staebler, G. M. 1
Stallard, B. W. 4
Stambaugh, R. D. 1
Stangeby, P. C. 71
Stav, R. D. 1
Stockdale R. E. 1
Strait, E. J. 1
Street, R. 1
Stroth, U. 52
Swain, D. W. 5
Sydora, R. D. 9
Synakowski, E. 8
Takahashi, H. 8
Takechi, M. 56
Takenaga, H. 56
Tang, W. 8
Taylor, P. L. 1
Taylor, T. S. 1
Temkin, R. J. 27
Terpstra, T. B. 1
Thomas, D. M. 1
Thomas, M. P. 1
Thomas, P. R. 44
Thompson, S. I. 1
Thurgood, P. A. 1
Tooker, J. F. 1
Trost, P. K. 1
Trukhin, V. 62
Tupper, M. 1
Turgarinov, S. 64
Turnbull, A. D. 1
Tynan, G. R. 33
Ulrickson, M. A. 9
Unterberg, B. 48
Vanderlann, J. 1
VanZeeland, M. A. 6
Vernon, R. 39
Visser, S. 1
VonGoeler, S. 8
Wade, M. R. 5
Waelbroeck, F. L. 37
Wagner, R. 33
Walker, M. L. 1
Waltz, R. E. 1
Wampler, W. R. 9
Wan, B. 65
Wang, G. 32
Wang, Z. 67
Warner, A. M. 1
Watkins, J. G. 9
Watson, G. W. 31
Watson, G. 31
Welander, A. S. 1
Weschenfelder, F. 48
Wesley, J. C. 1
West, W. P. 1
Whaley, J. 9
Whyte, D. G. 39
Wight, J. 1
Wilson, H. R. 53
Winter, J. 48
Wolf, N. S. 4
Wolf, R. 52
Wong, C. P. C. 1
Wong, K. -L. 8
Wong, S. K. 1
Wood, R. D. 4
Wròblewski, D. 16
Wu, X. 65
Xu, X. Q. 4
Yamaguchi, S. 15
Yin, F. 65
Yip, H. H. 1
You, K. I. 66
Zaniol, B. 54
Zeng, L. 32
Zerbini, M. 50
Zhang, C. 65
Zhang, D. 65
Zhang, J. 33
Zhou, D. 65
Zohm, H. 52
Zwicker, A. 24

AFFILIATIONS
OF THE DIII-D TEAM MEMBERS*

U. S. LABORATORIES
1 General Atomics, San Diego, CA
2 Argonne National Laboratory, Argonne, IL
3 Los Alamos National Laboratory, Los Alamos, NM
4 Lawrence Livermore National Laboratory, Livermore, CA
5 Oak Ridge National Laboratory, Oak Ridge, TN
6 Oak Ridge Institute of Science Education, Oak Ridge, TN
7 Oak Ridge Associated Universities, Oak Ridge, TN
8 Princeton Plasma Physics Laboratory, Princeton, NJ
9 Sandia National Laboratories, Albuquerque, NM
10 Sandia National Laboratories, Livermore, CA

INDUSTRIES
11 Communications and Power Industries, Palo Alto, CA
12 Comp-X, Del Mar, CA
13 FARTECH, Inc., San Diego, CA
14 Hitachi Ltd, Japan
15 Mitsumishi Electric Corp., Japan
16 ORINCON Corp, San Diego, CA
17 SAIC, San Diego, CA
18 Tech-X, Boulder, CO
19 Tomlab Optimization Inc. Willow Creek, CA

U.S. UNIVERSITIES
20 Colorado School of Mines, Golden , CO
21 Columbia University, New York, NY
22 Georgia Institute of Technology, Atlanta, GA
23 Hampton University, Hampton, VA
24 Johns Hopkins University, Baltimore, MD
25 Lehigh University, Bethlehem, PA
26 LLE, University of Rochester, NY
27 Massachusetts Institute of Technology, Cambridge, MA
28 Palomar College, San Marcos, CA
29 Rensselaer Polytechnic Institute, Troy, NY
30 University of California, Berkeley, CA
31 University of California, Irvine, CA
32 University of California, Los Angeles, CA
33 University of California, San Diego, CA
34 University of Illinois, Champaign, IL
35 University of Maryland, College Park, MD
36 University of New Mexico, Albuquerque, NM
37 University of Texas at Austin, Austin, TX
38 University of Washington, Seattle, WA
39 University of Wisconsin, Madison, WI

EUROPE
40 Chalmers University, Götteborg, Sweden.
41 Consorzio RFX, Padua, Italy
42 Culham Laboratory, Abingdon, UK
43 Ecole Polytechnique, Lausanne, Switzerland
44 EURATOM, CEA, Cadarache, France
45 EURATOM, CIEMAT, Madrid, Spain
46 EURATOM, Ecole Royale Militaire, Brussels, Belgium
47 EURATOM, IST, Lisbon, Portugal
48 EURATOM, Kernsforschunganlage, Jülich, Germany
49 FOM Inst., Rijnhuizen, The Netherlands
50 ENEA, Frascati, Italy
51 JET Joint Undertaking, Abingdon, Oxfordshire, UK
52 Max Planck Institute for Plasma Physics, Garching, Germany
53 UKAEA Fusion Culham Science Center, Abington, Oxon, UK
54 University of Padua, Padua, Italy
55 University of Paris, France

JAPAN
56 Japan Atomic Energy Research Insitute, Naka, Japan
57 Tsukuba University, Tsukuba, Japan
58 National Institute for Fusion Science, Toki, Japan
59 Kyoto University, Kyoto, Japan

RUSSIA
60 Efremov Institute, St. Petersburg, Russia
61 Keldysh Institute, Moscow, Russia
62 Kurchatov Institute, Moscow, Russia
63 Moscow State University, Moscow, Russia
64 Troitsk Institute, Troitsk, Russia

ASIA AND AUSTRALIA
65 Academia Sinica Institute of Plasma Physics, Heifei, China
66 Korea Basic Science Institute, Daejeon, Korea
67 Southwestern Institute of Physics, Sichuan, China
68 Dong Hua University, Haulien, Taiwan
69 Australian National University, Canberra, Australia

AMERICAS
70 CCFM, Varennes, Quebec, Canada
71 University of Toronto, Canada
72 University of Campinas, Brazil

* The affiliation at the time of the most recent collaboration with DIII-D is given.